Intrinsic persistent spin helix state in two-dimensional group-IV monochalcogenide MX monolayers (M = Sn or Ge and X = S, Se, or Te)

Moh. Adhib Ulil Absor[1,*] and Fumiyuki Ishii[2]
[1]*Department of Physics, Universitas Gadjah Mada, Sekip Utara, BLS 21 Yogyakarta, Indonesia*
[2]*Nanomaterial Research Institute, Kanazawa University, 920-1192, Kanazawa, Japan*

(Received 1 June 2019; revised manuscript received 2 August 2019; published 3 September 2019)

Energy-saving spintronics are believed to be implementable on systems hosting the persistent spin helix (PSH) since they support an extraordinarily long spin lifetime of carriers. However, achieving the PSH requires a unidirectional spin configuration in the momentum space, which is practically nontrivial due to the stringent conditions for fine-tuning the Rashba and Dresselhaus spin-orbit couplings. Here, we predict that the PSH can be intrinsically achieved on a two-dimensional (2D) group-IV monochalcogenide MX monolayer, a new class of the noncentrosymmetric 2D materials having in-plane ferroelectricity. Due to the C_{2v} point-group symmetry in the MX monolayer, a unidirectional spin configuration is preserved in the out-of-plane direction and thus maintains the PSH that is similar to the [110] Dresselhaus model in the [110]-oriented quantum well. Our first-principle calculations on various MX (M = Sn, Ge; X = S, Se, Te) monolayers confirmed that such typical spin configuration is observed, in particular, at near the valence-band maximum where a sizable spin splitting and a substantially small wavelength of the spin polarization are achieved. Importantly, we observe reversible out-of-plane spin orientation under opposite in-plane ferroelectric polarization, indicating that an electrically controllable PSH for spintronic applications is plausible.

DOI: 10.1103/PhysRevB.100.115104

I. INTRODUCTION

Recent development of spintronics relies on the new pathway for exploiting the electron's spin in semiconductors by utilizing the effect of spin-orbit coupling (SOC) [1,2]. In a system with a lack of inversion symmetry, the SOC induces an effective magnetic field, known as a spin-orbit field (SOF), acting on spin so that the effective SOC Hamiltonian can be expressed as

$$H_{\mathrm{SOC}} = \vec{\Omega}(\vec{k}) \cdot \vec{\sigma} = \alpha(\hat{E} \times \vec{k}) \cdot \vec{\sigma}, \tag{1}$$

where $\vec{\Omega}$ is the SOF vector, $\vec{k}$ is the wave vector representing the momentum of electrons, $\vec{\sigma} = (\sigma_x, \sigma_y, \sigma_z)$ is the Pauli matrices vector, and α is the strength of the SOC that is proportional to the magnitude of the local electric field $\vec{E}$ induced by the crystal inversion asymmetry. Since the SOF is odd in the electron's wave vector $\vec{k}$, as was first demonstrated by Dresselhaus [3] and Rashba [4], the SOC lifts Kramers' spin degeneracy and leads to a complex $\vec{k}$-dependent spin configuration of the electronic bands. In particular, interest is driven due to a possibility to manipulate this spin configuration by using an external electric field to create nonequilibrium spin polarization [5], leading to various important phenomena such as the spin Hall effect [6], spin galvanic effect [7], and spin ballistic transport [8], thus offering a realization of spintronics devices such as spin-field effect transistors (SFET) [9].

From a practical perspective, materials having strong Rashba SOC have generated significant interest since they allow for electrostatic manipulation of the spin states [1,10], paving the way towards non-charge-based computing and information processing [2]. However, strong SOC is also known to induce the undesired effect of causing spin decoherence [11], which plays an adverse role in the spin lifetime. In a diffusive transport regime, impurities and defects act as scatters which change the momentum of electrons and simultaneously randomize the spin due to the momentum-dependent SOF, leading to the fast spin decoherence through the Dyakonov-Perel (DP) mechanism of spin relaxation [11]. This process induces spin dephasing and a loss of the spin signal, such that the spin lifetime significantly reduces, thus limiting the performance of potential spintronic devices.

A possible way to overcome this obstacle is to eliminate the problem of spin dephasing by suppressing the DP spin relaxation. This can be achieved, in particular, by designing a structure where the SOF orientation is enforced to be unidirectional, preserving a unidirectional spin configuration in the momentum space. In such a situation, electron motion together with the spin precession around the unidirectional SOF leads to a spatially periodic mode of the spin polarization known as the persistent spin helix (PSH) [12,13]. The corresponding spin-wave mode protects the spins of electrons from dephasing due to SU(2) spin rotation symmetry, which is robust against spin-independent scattering and renders an extremely long spin lifetime [12,14]. Previously, the PSH was demonstrated on various [001]-oriented semiconductors quantum wells (QWs) [15–20] having an equal strength of the Rashba and Dresselhaus SOC or on [110]-oriented semiconductor QW [21] in which the SOC is described by the [110] Dresselhaus model. Here, for the former, the spin configurations are enforced to be unidirectional in the in-plane [110] direction, whereas for the latter, they are oriented in the out-of-plane [001] direction. Similar to the [110]-oriented QW, the

*adib@ugm.ac.id

 ©2019 American Physical Society

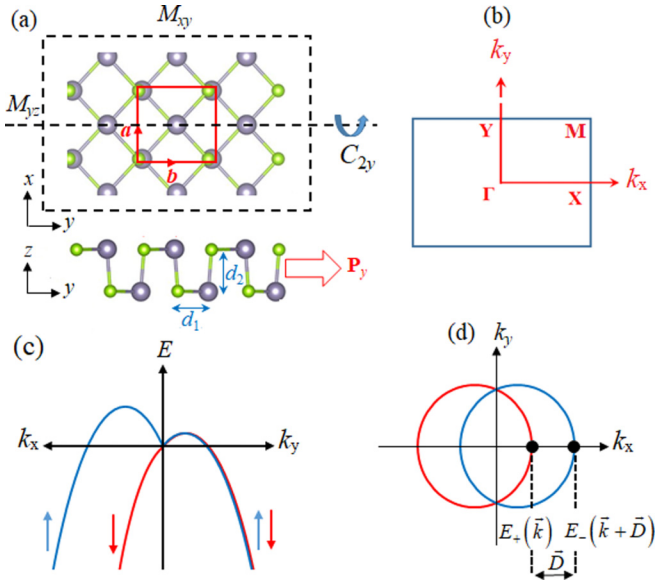

FIG. 1. (a) Atomic structure of the MX monolayer corresponding to it symmetry operations. Black and green balls represent the M (M = Sn, Ge) and X (X = S, Se, Te) atoms, respectively. The unit cell of the crystal is indicated by red lines characterized by a and b lattice parameters in the x and y directions. d_1 and d_2 represent bond length between the M (M = Sn, Ge) and X (X = S, Se, Te) atoms in the in-plane and out-of-plane directions, respectively. (b) First Brillouin zone of the MX monolayer characterized by high-symmetry $\vec{k}$ points (Γ, Y, M, X) are shown. (c) Spin-split bands induced by the SOC and C_{2v} point-group symmetry and (d) the corresponding Fermi contours in the momentum space are schematically shown. Here, the Fermi contours are characterized by two Fermi loops shifted by the wave vector $\vec{D}$, exhibiting a unidirectional spin configuration in the out-of-plane direction. The red and blue lines (or arrows) represent positive and negative spins, respectively, in the out-of-plane directions.

PSH state has recently been reported for the $LaAlO_3/SrTiO_3$ interface [22], the ZnO [10-10] surface [23], halogen-doped SnSe monolayers [24], and WO_2Cl_2 monolayers [25]. Although the PSH has been widely studied on various QW systems [15–20], it is practically nontrivial due to the stringent conditions for fine-tuning the Rashba and Dresselhaus SOCs. Therefore, it would be desirable to find a new class of material which intrinsically supports the PSH.

In this paper, we show that the PSH can be intrinsically achieved on a two-dimensional (2D) group-IV monochalcogenide MX monolayer, a new class of noncentrosymmetric 2D materials having in-plane ferroelectricity [26–30]. On the basis of density-functional theory (DFT) calculations on various MX (M = Sn, Ge; X = S, Se, Te) monolayers, supplemented with symmetry analysis, we find that a unidirectional spin orientation is preserved in the out-of-plane direction, yielding a PSH that is similar to the [110] Dresselhaus model in the [110]-oriented QW. Such typical spin configuration is observed, in particular, near the valence-band maximum, having a sizable spin splitting and small wavelength of the spin polarization. More interestingly, we observe reversible out-of-plane spin orientation under opposite in-plane ferroelectric polarization, suggesting that an electrically controllable PSH is achievable, which is useful for spintronic applications.

TABLE I. Structural-related parameters corresponding to the band gap of the MX monolayer. a and b (in Å) represent the lattice parameters in the x and y directions, respectively. d_1 and d_2 (in Å) indicate the bond length between the M (M = Sn, Ge) and X (X = S, Se, Te) atoms in the in-plane and out-of-plane directions, respectively. E_g (in eV) represents the energy gap where the star (*) indicates a direct band gap.

MX monolayer	a (Å)	b (Å)	d_1 (Å)	d_2 (Å)	E_g (eV)
SnS	4.01	4.39	2.71	2.63	1.38
SnSe	4.34	4.49	2.89	2.7	0.98*
SnTe	4.54	4.58	3.31	3.04	0.85
GeS	3.68	4.40	2.53	2.46	1.45
GeSe	3.99	4.26	2.72	2.57	1.10*
GeTe	4.27	4.47	2.95	2.81	0.92

II. COMPUTATIONAL DETAILS

We performed first-principles calculations by using DFT within the generalized gradient approximation (GGA) [31] implemented in the OPENMX code [32]. Here, we adopted norm-conserving pseudopotentials [33] with an energy cutoff of 350 Ry for charge density. The $12 \times 12 \times 1$ k-point mesh was used. The wave functions were expanded by linear combination of multiple pseudoatomic orbitals generated by using a confinement scheme [34,35], where two s-, two p-, two d-character numerical pseudoatomic orbitals were used. The SOC was included in the DFT calculations by using j-dependent pseudopotentials [36]. The spin textures in the momentum space were calculated by using the spin density matrix of the spinor wave functions obtained from the DFT calculations as we applied recently on various 2D materials [23,24,37–40].

In our DFT calculations, we considered ferroelectric phase of the MX monolayer having black phosphorene-type structure [41,42]. The minimum-energy pathways of ferroelectric transitions were calculated by using nudged elastic band (NEB) method [43] based on the interatomic forces and total energy obtained from DFT calculations. The ferroelectric polarization was calculated by using the Berry-phase approach [44], where both electronic and ionic contributions were considered. We used a periodic slab to model the MX monolayer, where a sufficiently large vacuum layer (20 Å) is applied in order to avoid interaction between adjacent layers. We used the axes system where layers are chosen to sit on the x-y plane, while the x axis is taken to be parallel to the puckering direction [Fig. 1(a)]. The geometries were fully relaxed until the force acting on each atom was less than 1 meV/Å. The optimized structural-related parameters are summarized in Table I and are in good agreement overall with previously reported data [29,41,45].

III. RESULTS AND DISCUSSION

A. Symmetry-protected persistent spin helix state in MX monolayer

To predict the PSH state in the MX monolayer (ML), we first derive an effective low-energy Hamiltonian by using symmetry analysis. As shown in Fig. 1(a), the crystal structures of the MX ML has black phosphorene-type structures where the symmetry group is isomorphic to the C_{2v}^7 or $Pmn2_1$

TABLE II. Transformation rules for the in-plane wave-vector components (k_x, k_y) and spin Pauli matrices $(\sigma_x, \sigma_y, \sigma_z)$ under the considered point-group symmetry operations. Time-reversal symmetry, implying a reversal of both spin and momentum, is defined as $T = i\sigma_y K$, where K is the complex conjugation, while the point-group operations are defined as $\hat{C}_{2y} = i\sigma_y$, $\hat{M}_{yz} = i\sigma_x$, and $\hat{M}_{xy} = i\sigma_z$.

Symmetry operation	(k_x, k_y)	$(\sigma_x, \sigma_y, \sigma_z)$
$\hat{T} = i\sigma_y K$	$(-k_x, -k_y)$	$(-\sigma_x, -\sigma_y, -\sigma_z)$
$\hat{C}_{2y} = i\sigma_y$	$(-k_x, k_y)$	$(-\sigma_x, \sigma_y, -\sigma_z)$
$\hat{M}_{yz} = i\sigma_x$	$(-k_x, k_y)$	$(\sigma_x, -\sigma_y, -\sigma_z)$
$\hat{M}_{xy} = i\sigma_z$	(k_x, k_y)	$(-\sigma_x, -\sigma_y, \sigma_z)$

space group [41,42]. There are four symmetry operations in the crystal lattice of the MX monolayer [Fig. 1(a)]: (i) identity operation E; (ii) twofold screw rotation $\tilde{C}_{2y}$ (twofold rotation around the y axis, C_{2y}, followed by translation of $\tau = a/2, b/2$), where a and b are the lattice parameters along the $\vec{a}$ and $\vec{b}$ directions, respectively; (iii) glide reflection $\tilde{M}_{xy}$ (reflection with respect to the xy plane followed by translation τ); and (iv) reflection M_{yz} with respect to the yz plane. The effective $\vec{k} \cdot \vec{p}$ Hamiltonian can be constructed by taking into account all symmetry operations in the little group of the wave vector in the reciprocal space.

Let Q be a high-symmetry point in the first Brillouin zone (FBZ) where a pair of spin-degenerate eigenstates exists in the valence band maximum (VBM) or conduction-band minimum (CBM). This degeneracy appears due to time-reversal symmetry T for which the condition $\vec{Q} = -\vec{Q} + \vec{G}$ is satisfied, where $\vec{G}$ is the 2D reciprocal-lattice vector. Such points are located at the center of the FBZ (Γ point), or some points that are located at the boundary of the FBZ such as X, Y, and M points for a primitive rectangular lattice [Fig. 1(b)]. The band dispersion around the Q point can be deduced by identifying all symmetry-allowed terms so that $O^{\dagger}H(k)O = H(k)$ is obtained, where O denotes all symmetry operations belonging to the little group of the Q point, supplemented by time-reversal symmetry T.

For simplicity, let us assume that the little group of the wave vector $\vec{k}$ at the Q point belongs to the C_{2v} point group similar to that of the crystal in the real space. Therefore, the wave vector $\vec{k}$ and spin vector $\vec{\sigma}$ can be transformed according to the symmetry operation O in the C_{2v} point group and time-reversal symmetry T. The corresponding transformation for the $\vec{k}$ and $\vec{\sigma}$ are listed in Table II. Collecting all terms which are invariant with respect to the symmetry operation, we obtain the following effective Hamiltonian up to third-order correction of k [13]:

$$\begin{aligned} H &= E_0(k) + \alpha k_x \sigma_z + \left(\alpha' k_y^2 k_x + \alpha'' k_x^3\right)\sigma_z \\ &= E_0(k) + \alpha^{(1)} k \cos\theta \sigma_z + \alpha^{(3)} k \cos(3\theta)\sigma_z, \end{aligned} \tag{2}$$

where $E_0(k) = \hbar^2(k_x^2 + k_y^2)/2m^*$ is the nearly-free-electron or -hole energy, $\alpha^{(1)}$ defined as $\alpha^{(1)} = \alpha + (k^2/4)(\alpha' + 3\alpha'')$ originates from the contribution of the k-linear parameter α and the correction provided by the third-order parameters (α' and α''), $\alpha^{(3)}$ corresponds to the third-order parameters by the relation $\alpha^{(3)} = (1/4)[\alpha' - \alpha'']k^2$, and θ is the angle of the momentum $\vec{k}$ with respect to the x axis defined as $\theta = \cos^{-1}(k_x/k)$. Solving the eigenvalue problem involving the Hamiltonian of Eq. (2) yields split-split energy dispersions:

$$E_{\pm} = E_0(k) \pm [\alpha^{(1)} \cos\theta + \alpha^{(3)} \cos(3\theta)]k. \tag{3}$$

These dispersions are schematically illustrated in Fig. 1(c), showing a highly anisotropic spin splitting.

Since the Hamiltonian (2) is only coupled with σ_z, neglecting all the cubic terms leads to the SU(2) symmetry of the Hamiltonian [12,13],

$$H = E_0(k) + \alpha k_x \sigma_z, \tag{4}$$

with the energy dispersions

$$E_{\pm} = E_0(k) \pm \alpha k_x. \tag{5}$$

Importantly, these dispersions have the shifting property: $E_+(\vec{k}) = E_-(\vec{k} + \vec{D})$, where $\vec{D} = 2m^*\alpha(1, 0, 0)/\hbar^2$ is the shifting wave vector. As a result, a constant-energy cut shows two Fermi loops whose centers are displaced from their original point by $\mp\vec{D}$, as schematically shown in Fig. 1(d).

Since the z component of the spin operator S_z commutes with the Hamiltonian (4), $[S_z, H] = 0$, the spin operator S_z is a conserved quantity. Here, the expectation value of the spin $\langle S \rangle$ only has the out-of-plane component: $(\langle S_x \rangle, \langle S_y \rangle, \langle S_z \rangle)_{\pm} = \pm(\hbar/2)(0, 0, 1)$ at any wave vector $\vec{k}$ except for $k_x = 0$, resulting in the unidirectional out-of-plane spin configuration in momentum space [Fig. 1(d)]. In such a situation, the unidirectional out-of-plane SOF is achieved, implying that the electron motion accompanied by the spin precession around the SOF form a spatially periodic mode of the spin polarization, yielding the PSH, which is similar to the [110] Dresselhaus model [12] as recently demonstrated on the [110]-oriented semiconductor QW [21].

In the next section, we discuss our results from the first-principles DFT calculations on various MX (M = Sn, Ge; X = S, Se, Te) monolayers to confirm the above-predicted PSH.

B. Density-functional theory analysis of MX monolayer

Figure 2 shows the electronic band structures of various MX (M = Sn, Ge; X = S, Se, Te) monolayers calculated along the selected $\vec{k}$ paths in the FBZ corresponding to the density of states (DOS) projected to the atomic orbitals. Without including the SOC, it is evident that there are two equivalent extremum valleys characterizing the valence-band maximum (VBM) and conduction-band minimum (CBM) located at the points that are not time-reversal invariant. Consistent with previous calculations [29,41,45], the MX monolayers show an indirect band gap (except for the MSe monolayer), where the VBM and CBM are located along the Γ-Y and Γ-X lines, respectively. Overall, the calculated band gap [see Table I] is in a good agreement with previous results under the GGA-PBE level [41,45]. Our calculated results for the DOS projected to the atomic orbitals confirm that the M-s and X-p orbitals contribute dominantly to the VBM, while the CBM mainly originates from the contribution of the M-p and X-s orbitals.

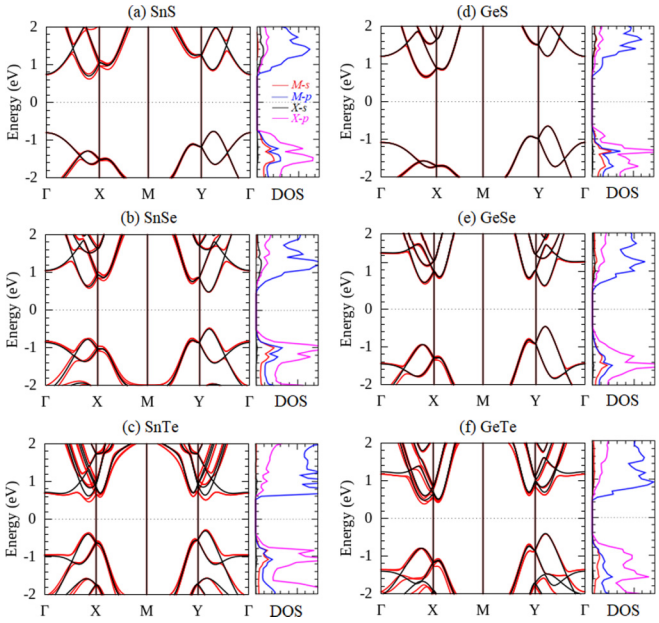

FIG. 2. (a) Electronic band structure of the MX monolayers corresponding to the density of state projected to the atomic orbitals for (a) SnS, (b) SnSe, (c) SnTe, (d) GeS, (e) GeSe, and (f) GeTe. The black and red lines show the calculated band structures without and with the SOC, respectively.

Turning the SOC strongly modifies the electronic band structures of the MX monolayers (Fig. 2). Importantly, a sizable splitting of the bands produced by the SOC is observed at some high-symmetry $\vec{k}$ points and along certain $\vec{k}$ paths in the FBZ. This splitting is especially pronounced around the X and Y points near both the VBM and CBM. However, there are special high-symmetry lines and points in the FBZ where the splitting is zero. This is, in particular, the case for the Γ-Y line, where the wave vector $\vec{k} = (0, k_y, 0)$ is parallel to the ferroelectric polarization along the y direction.

To analyze the properties of the spin splitting, we consider SnTe monolayer as a representative example of the MX monolayer. Here, we focus our attention on the bands near the VBM (including spin) around the Y point due to the large spin splitting as highlighted by the blue lines in Fig. 3(a). Without the SOC, it is clearly seen from the band dispersion that the fourfold degenerate state is visible at the Y point [Fig. 3(b)].

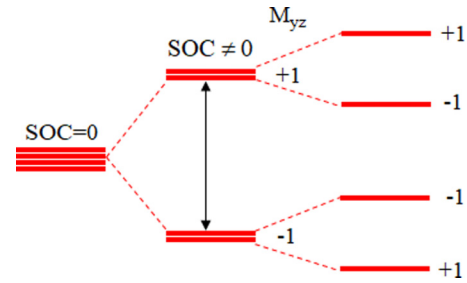

FIG. 4. Schematic view of the energy level around the Y point near the VBM. The SOC splits the states into two doublets with eigenvalues of $M_{yz} = \pm 1$, which are further split into a singlet with sign-reversed expectation values of spin.

Taking into account the SOC, this degeneracy splits into two pair doublets with the splitting energy of $\Delta E_Y = 9.2$ meV [Fig. 3(c)]. Although these doublets remain at $\vec{k}$ along the Γ-Y line, they split into a singlet when moving away along the Y-M line, yielding a highly anisotropic spin splitting.

To clarify the origin of the anisotropic splitting around the Y point near the VBM, we discuss our system based on a symmetry argument. At the Y point, the little group of the wave vector $\vec{k}$ belongs to the C_{2v} point group [42]. As previously mentioned, the C_{2v} point group contains the C_{2y} rotation symmetry around the y axis. Applying the C_{2y} rotation twice to the Bloch wave function, we have $C_{2y}^2 \psi_k = e^{ik_y b} \psi_k$, so we obtain $C_{2y}^2 = e^{ik_y b}$. We further define an antiunitary symmetry operator, $\Theta = C_{2y} T$, so that $\Theta^2 = C_{2y}^2 T^2 = -e^{ik_y b}$ for a spin half system. Therefore, at the Y point ($k_y = \pi/b$), we find that $\Theta^2 = -1$, so the Bloch states $(\psi_k, \Theta\psi_k)$ are double degenerate.

In addition, there is also M_{yz} mirror symmetry in the C_{2v} point group, which commutes with the Hamiltonian of the crystal, $[M_{yx}, H] = 0$. By operating M_{yz} symmetry to the Bloch states, we find that $M_{yz}^2 = -e^{-ik_y b}$. Accordingly, the Bloch states can be labeled by using the M_{yz} eigenvalues, i.e., $M_{yz}|\psi_k^{\pm}\rangle = \pm ie^{ik_y b/2}|\psi_k^{\pm}\rangle$. Here, for the Y point ($k_y = \pi/b$), we find that $M_{yz}^2 = 1$, so we obtain $M_{yz}\psi_Y^{\pm} = \pm\psi_Y^{\pm}$ and $M_{yz}\Theta\psi_Y^{\pm} = \pm\Theta\psi_Y^{\pm}$. Therefore, there are two conjugated doublets at the Y point, $(\psi_Y^+, \Theta\psi_Y^+)$ or $(\psi_Y^-, \Theta\psi_Y^-)$, which are distinguished by the M_{yz} eigenvalues, as schematically shown in Fig. 4. These conjugated doublets are preserved along the

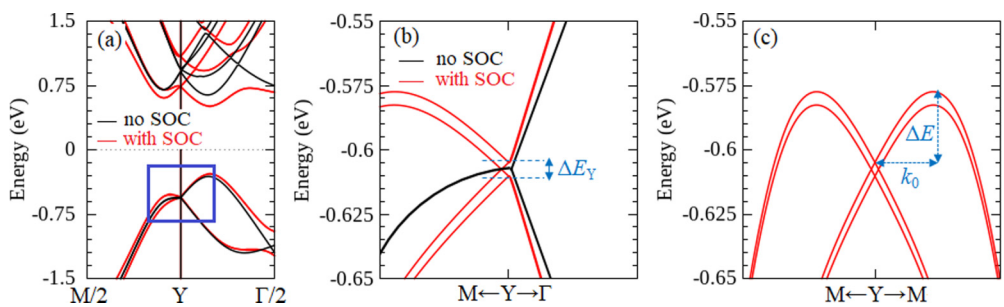

FIG. 3. (a) Energy-band dispersion of SnTe monolayer along the M-Y-Γ lines calculated without (black lines) and with (red lines) the SOC. (b) Zoom-in on the energy dispersion near the VBM close to the Y point along M-Y and Y-Γ lines, as highlighted by the blue lines in panel (a). (c) Spin-splitting properties of the bands around the Y point along the M-Y-M lines characterized by (i) splitting energy (ΔE), i.e., the energy difference between the VBM along the Y-M line and the energy at the Y point, and (ii) momentum offset (k_0).

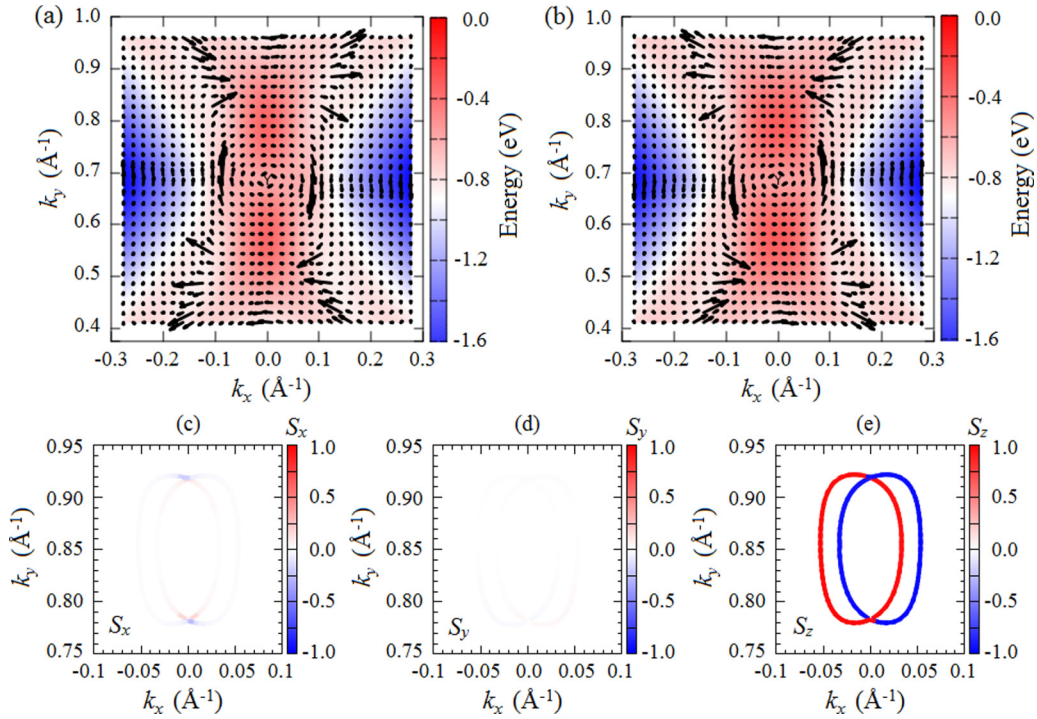

FIG. 5. Energy profiles of the spin textures calculated around the Y point for (a) outer and (b) inner branches in the spin-split bands near the VBM. The color scale in panels (a) and (b) indicate the energy band. Constant-energy contours corresponding to a cut 1 meV below the VBM characterized by (c) S_x, (d) S_y, and (e) S_z components of the spin distribution are shown. The color scale in panels (c)–(e) show the modulus of the spin polarization.

Γ-Y line but they split into singlets when moving to the Y-M line, which are protected by the M_{yz} and C_{2y} symmetry operations. As a result, a strong anisotropic splitting is achieved, which is in fact consistent well with our DFT results shown in Fig. 3(c).

To further demonstrate the nature of the observed anisotropic splitting around the Y point near the VBM, we show in Figs. 5(a) and 5(b) the energy profiles of the spin textures for the outer and inner branches in the spin-split bands, respectively. It is found that a complex pattern of the spin polarization is observed around the Y point, which is remarkably different either from Rashba- and Dresselhaus-like spin textures. This is in contrast with the widely studied 2D materials such as $PtSe_2$ [37,46], BiSb [47], $LaOBiS_2$ [48], and polar transition-metal dichalcogenide [39,40], where the Rashba-like spin textures are identified. In particular, we observe a uniform spin polarization at the energy close to the VBM, which persists in a region located about 0.1 Å^{-1} from the Y point along the Y-M (k_x) and Y-Γ (k_y) lines [see the region with red color in Figs. 5(a) and 5(b)]. By carefully analyzing the spin textures measured at the constant-energy cut of 1 meV below the VBM, we confirmed that this peculiar spin polarization is mostly dominated by the out-of-plane component S_z [Fig. 5(e)] rather than the in-plane ones (S_x, S_y) [Figs. 5(c) and 5(d)], leading to the unidirectional out-of-plane spin textures. On the other hand, the constant-energy cut also induces the Fermi lines characterized by the shifted two circular loops along the Y-M (k_x) direction and the degenerate nodal point along the Y-Γ (k_y) direction. Both the spin textures and Fermi lines agree well with our $\vec{k}\cdot\vec{p}$ Hamiltonian model derived from the symmetry analysis. Since the spin textures are uniformly oriented in the out-of-plane direction, the unidirectional out-of-plane SOF is achieved, maintaining the PSH, which is similar to the [110] Dresselhaus model [12]. Therefore, it is expected that the DP mechanism of the spin relaxation is suppressed, potentially ensuring to induce an extremely long spin lifetime.

For a quantitative analysis of the above-mentioned spin splitting, we here calculate the strength of the spin splitting by evaluating the band dispersions along the Y-M and the Y-Γ directions near the VBM in terms of the effective $\vec{k}\cdot\vec{p}$ Hamiltonian model given in Eq. (2). Here, according to Eq. (3), the spin-splitting energy ($E_{\mathrm{Split}} = E_+ - E_-$) can be formulated as

$$E_{\mathrm{Split}} = 2k[(\alpha + (k^2/4)(\alpha' + 3\alpha'')\cos\theta + (k^2/4)(\alpha' - \alpha'')\cos(3\theta)]. \quad (6)$$

The parameters α, α', and α'' can be calculated by numerically fitting Eq. (6) to the spin-splitting energy along the Y-M (k_x) and the Y-Γ (k_y) directions obtained from our DFT results, and we find that $\alpha = 1.23$ eV Å, $\alpha' = 0.0014$ eV Å^3, and $\alpha'' = 0.0027$ eV Å^3. It is clearly seen that the obtained value of the cubic term parameters (α', α'') is too small compared with that of the linear-term parameter α, indicating that the contribution of the higher-order correction is not essential. On the other hand, by using the energy dispersion of Eq. (5), we also obtain the linear-term parameter α through the relation $\alpha = 2E_R/k_0$, where E_R and k_0 are the shifting energy and the wave vector as illustrated in Fig. 3(c). This reveals that the calculated value

TABLE III. Spin-splitting parameter α (in eV Å) and the wavelength of the spin polarization λ (in nm) for the selected PSH materials.

Systems	α (eV Å)	λ (nm)	Reference
MX monolayer			
SnS	0.09	1.5×10^2	This work
SnSe	0.74	44.85	This work
SnTe	1.20	7.13	This work
GeS	0.071	8.9×10^2	This work
GeSe	0.57	91.84	This work
GeTe	1.67	1.82	This work
Interface			
GaAs/AlGaAs	$(3.5–4.9) \times 10^{-3}$	$(7.3–10) \times 10^3$	Ref. [16]
	2.77×10^{-3}	5.5×10^3	Ref. [17]
InAlAs/InGaAs	1.0×10^{-3}		Ref. [18]
	2.0×10^{-3}		Ref. [20]
$LaAlO_3/SrTiO_3$	7.49×10^{-3}	0.098×10^2	Ref. [22]
Surface			
ZnO(10-10) surface	34.78×10^{-3}	1.9×10^2	Ref. [23]
Bulk			
$BiInO_3$	1.91	2.0	Ref. [49]
2D monolayer			
Halogen-doped SnSe	1.6–1.76	1.2–1.41	Ref. [24]
WO_2Cl_2	0.9		Ref. [25]

of α is 1.20 eV Å, which in fair agreement with that obtained from the higher-order-correction model. Since the spin splitting is dominated by the linear term, ignoring the higher-order-correction preserves the SU(2) symmetry of the Hamiltonian, thus maintaining the PSH as we expected.

It is important to note here that the PSH predicted in the present system should ensure that a spatially periodic mode of spin polarization is achieved. The corresponding spin-wave mode is characterized by the wavelength of the spin polarization defined as [12] $\lambda = (\pi\hbar^2)/(m^*\alpha)$, where m^* is the hole effective mass. Here, the effective mass m^* can be evaluated by fitting the sum of the band dispersions along the Y-M direction in the VBM. Here, we find that $m^* = 0.056m_0$, where m_0 is the free-electron mass, which is in good agreement with previous results reported by Xu *et al.* [45] The resulting wavelength λ is 7.13 nm, which is typically on the scale of the lithographic dimension used in the recent semiconductor industry [50].

We summarize the calculated results of the α and λ in Table III and compare the results with a few selected PSH materials from previously reported data. It is found that the calculated value of α in various *MX* monolayer is much larger than that observed in various QWs such as GaAs/AlGaAs [16,17] and InAlAs/InGaAs [18,20], ZnO (10-10) surfaces [23], and strained LaAlO3/SrTiO3 (001) interfaces [22]. However, this value is comparable with those observed on the bulk $BiInO_3$ [49], halogen-doped SnSe monolayer [24], and WO_2Cl_2 monolayer [25]. The associated spin-splitting parameters are sufficient to support the functionality of room-temperature spintronics. On the other hand, we observed a small wavelength λ (in nm scale) of the spin polarization, which is in fact two orders less than that observed in the GaAs/AlGaAs QW [16,17], which means that the present system is promising for nanoscale spintronics devices.

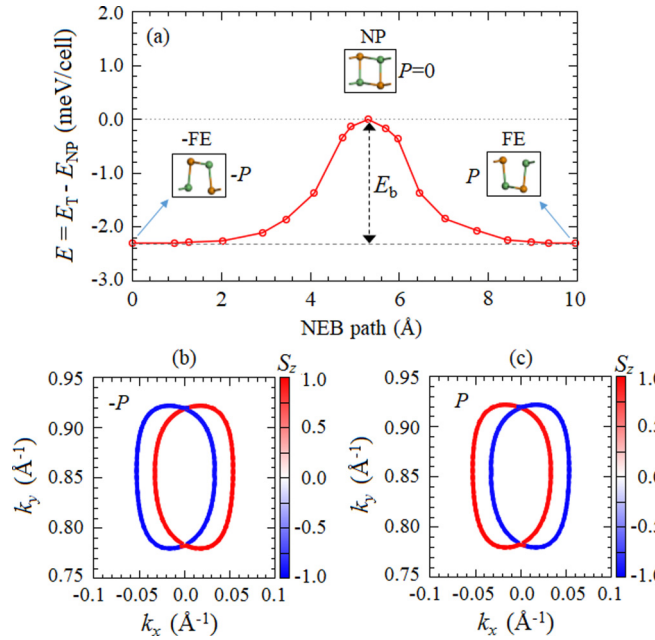

FIG. 6. (a) Nudged elastic band calculation for the polarization switching process through centrosymmetric (paraelectric) structures in SnTe monolayer. Two ferroelectric structures (FE) in the ground state with opposite direction of the in-plane electric polarization and a paraelectric structure with zero electric polarization (NP) are shown. E_b is the barrier energy defined as the difference between the total energy of the ferroelectric (E_T) and paraelectric (E_{NP}) structures. Reversible out-of-plane spin orientation in SnTe monolayer calculated at 1 meV below the VBM for the ferroelectric structure with opposite in-plane polarization: (b) $-P$ and (c) P.

Now, we discuss our prediction of the PSH, which is associated with the ferroelectricity in the *MX* monolayer. As previously mentioned, the *MX* monolayer possesses in-plane ferroelectricity [26–30], which is induced by the in-plane atomic distortion in the real space of the crystal [see Fig. 1(a)]. Therefore, a substantial electric polarization in the in-plane direction is established. For instant, our Berry-phase calculation [44] on a SnTe monolayer revealed that the magnitude of the in-plane electric polarization is 13.8 μC/cm^2 when an effective thickness of 1 nm is used for a monolayer, which is in good agreement with a previous result [29]. Importantly, we predict the feasibility of polarization switching in SnTe monolayers by analyzing the minimum-energy pathway of the ferroelectric transition calculated by using the NEB method [43]. As shown in Fig. 6(a), we find that the calculated barrier energy for polarization switching process is 2.26 meV/cell in the SnTe monolayer. This value is comparable to those of the 2D ferroelectric reported in previous work [25,26] but is much smaller than that in conventional ferroelectric $BaTiO_3$ [51], suggesting that a switchable in-plane ferroelectric polarization is plausible. Indeed, polarization switching in various *MX* monolayers by using an external electric field or strain effects has recently been reported [30]. Moreover, the barrier energy found in our system is much lower than the typical thermal energy (≈25.9 meV) at room temperature, indicating

that polarization switching can be maintained at below room temperature. This is also consistent with the fact that the low Curie temperature ($T_c = 270$ K) in SnTe monolayers has been experimentally reported [52].

By switching the in-plane ferroelectric polarization $\vec{P}$ in an MX monolayer, e.g., by applying an external electric field, a full reversal of the out-of-plane spin orientation can be expected. This is due to the fact that switching the in-plane ferroelectric polarization from $\vec{P}$ to $-\vec{P}$ is equivalent to the space inversion operation, which changes the wave vector from $\vec{k}$ to $-\vec{k}$, but preserves the spin vector $\vec{\sigma}$ [53,54]. Suppose that $|\psi_{\vec{P}}(\vec{k})\rangle$ is the Bloch state of the crystal with ferroelectric polarization $\vec{P}$. Under the space inversion operation I, both the polarization $\vec{P}$ and the wave vector $\vec{k}$ are reversed so that $I|\psi_{\vec{P}}(\vec{k})\rangle = |\psi_{-\vec{P}}(-\vec{k})\rangle$. However, application of time-reversal symmetry T reverses only $\vec{k}$, while $\vec{P}$ remains unchanged, leading to the fact that $TI|\psi_{\vec{P}}(\vec{k})\rangle = |\psi_{-\vec{P}}(\vec{k})\rangle$. The expectation values of spin operator $\langle S\rangle$ can now be calculated by

$$\begin{aligned}\langle S\rangle_{-\vec{P},\vec{k}} &= \langle\psi_{-\vec{P}}(\vec{k})|S|\psi_{-\vec{P}}(\vec{k})\rangle \\ &= \langle\psi_{\vec{P}}(\vec{k})|I^{-1}T^{-1}STI|\psi_{\vec{P}}(\vec{k})\rangle \\ &= \langle\psi_{\vec{P}}(\vec{k})|(-S)|\psi_{\vec{P}}(\vec{k})\rangle \\ &= \langle -S\rangle_{\vec{P},\vec{k}}, \end{aligned} \tag{7}$$

which indicates that the spin orientation can be reversed by switching the ferroelectric polarization. This analysis is in fact confirmed by our calculated results of the spin textures shown in Figs. 6(b) and 6(c), where the full reversal of the out-of-plane spin orientation is achieved under opposite in-plane ferroelectric polarization. Such an interesting property indicates that an electrically controllable PSH in an MX monolayer can be realized, which is very useful for operation in spintronic devices.

Thus far, we have predicted that the PSH with large spin splitting is achieved in the MX monolayer. In particular, the GeTe monolayer is promising for spintronics since it has the largest strength of the spin splitting ($\alpha = 1.67$ eV Å) of the MX monolayers. Because the PSH is achieved on the spin-split bands near the VBM [Fig. 3(a)], p-type doping for spintronics is expected to be realized. Moreover, by hole doping into the valence band of the MX monolayer, it is possible to map the formation and evolution of the PSH state by using near-filled scanning Kerr microscopy [55], which allows us to resolve the features down to tens-nm scale with sub-nanosecond time resolution. Finally, the hole-doped MX monolayer can also be applied to explore current-induced spin polarization, which is known as the Edelstein effect [56] and associated spin-orbit torque [57], indicating that the present system is promising for spintronic devices.

IV. CONCLUSION

In summary, by using first-principles DFT calculations, supplemented with symmetry analyses, we investigated the effect of SOC on the electronic structures of MX monolayers. We found that, due to C_{2v} point-group symmetry in the MX monolayer, the unidirectional out-of-plane spin configurations are preserved, inducing the PSH state that is similar to the [110] Dresselhaus model [12] observed on the [110]-oriented semiconductor QW. Our first-principle calculations on various MX (M = Sn, Ge; X = S, Se, Te) monolayers confirmed that this PSH is observed near the VBM, supporting large spin splitting and a small wavelength of the spin polarization. More importantly, we observed a reversible out-of-plane spin orientations under opposite in-plane ferroelectric polarization, indicating that an electrically controllable PSH in an MX monolayer can be realized, which is promising for spintronic devices.

Recently, there have been a number of other 2D materials that were predicted to maintain the in-plane ferroelectricity and the C_{2v} symmetry of the crystals. Therefore, it opens a possibility to further explore the achievable PSH states in these materials. Among them are those from the 2D elemental group- V (As, Sb, and Bi) monolayer with the puckered lattice structure [58,59]. Therefore, it is expected that our predictions will stimulate further theoretical and experimental efforts in the exploration of the PSH state in the 2D-based ferroelectric materials, broadening the range of the 2D materials for future spintronic applications.

ACKNOWLEDGMENTS

The first author (M.A.U.A.) would like to thank the Nanomaterial Research Institute, Kanazawa University, Japan, for providing financial support during his research visit. This work was partly supported by Grants-in-Aid on Scientific Research (Grant No. 16K04875) from the Japan Society for the Promotion of Science (JSPS) and a JSPS Grant-in-Aid for Scientific Research on Innovative Areas "Discrete Geometric Analysis for Materials Design" (Grant No. 18H04481). Part of this research was supported by a PDUPT Research Grant (No. 2627/UN1.DITLIT/DIT-LIT/LT/2019) from the Ministry of Research and Technology and Higher Education (RISTEK-DIKTI), Republic of Indonesia. The computations in this research were performed using the computer facilities at Gadjah Mada University, Indonesia, and the supercomputers at RIIT, Kyushu University, Japan.

[1] J. Nitta, T. Akazaki, H. Takayanagi, and T. Enoki, Phys. Rev. Lett. **78**, 1335 (1997).

[2] A. Manchon, H. C. Koo, J. Nitta, S. M. Frolov, and R. A. Duine, Nat. Mater. **14**, 871 (2015).

[3] G. Dresselhaus, Phys. Rev. **100**, 580 (1955).

[4] E. I. Rashba, Fiz. Tverd. Tela (Leningrad) **2**, 1224 (1960) [Sov. Phys. Solid State **2**, 1109 (1960)].

[5] S. Kuhlen, K. Schmalbuch, M. Hagedorn, P. Schlammes, M. Patt, M. Lepsa, G. Güntherodt, and B. Beschoten, Phys. Rev. Lett. **109**, 146603 (2012).

[6] X.-L. Qi, Y.-S. Wu, and S.-C. Zhang, Phys. Rev. B **74**, 085308 (2006).

[7] S. D. Ganichev, E. L. Ivchenko, V. V. Bel'kov, S. A. Tarasenko, M. Sollinger, D. Weiss, W. Wegscheider, and W. Prettl, Nature (London) **417**, 153 (2002).

[8] J. P. Lu, J. B. Yau, S. P. Shukla, M. Shayegan, L. Wissinger, U. Rössler, and R. Winkler, Phys. Rev. Lett. **81**, 1282 (1998).

[9] S. Datta and B. Das, Appl. Phys. Lett. **56**, 665 (1990).

[10] P. Chuang, S.-H. Ho, L. W. Smith, F. Sfigakis, M. Pepper, C.-H. Chen, J.-C. Fan, J. P. Griffiths, I. Farrer, H. E. Beere, G. A. C. Jones, D. A. Ritchie, and T.-M. Chen, Nat. Nanotechnol. **10**, 35 (2009).

[11] M. I. Dyakonov and V. I. Perel, Fiz.Tverd.Tela (Leningrad) **13**, 3581 (1971) [Sov. Phys. Solid State **13**, 3023 (1972)].

[12] B. A. Bernevig, J. Orenstein, and S.-C. Zhang, Phys. Rev. Lett. **97**, 236601 (2006).

[13] J. Schliemann, Rev. Mod. Phys. **89**, 011001 (2017).

[14] P. Altmann, M. P. Walser, C. Reichl, W. Wegscheider, and G. Salis, Phys. Rev. B **90**, 201306(R) (2014).

[15] J. D. Koralek, C. P. Weber, J. Orenstein, B. A. Bernevig, S.-C. Zhang, S. Mack, and D. D. Awschalom, Nature (London) **458**, 610 (2009).

[16] M. P. Walser, C. Reichl, W. Wegscheider, and G. Salis, Nat. Phys. **8**, 757 (2012).

[17] C. Schönhuber, M. P. Walser, G. Salis, C. Reichl, W. Wegscheider, T. Korn, and C. Schüller, Phys. Rev. B **89**, 085406 (2014).

[18] J. Ishihara, Y. Ohno, and H. Ohno, Appl. Phys. Express **7**, 013001 (2014).

[19] M. Kohda, V. Lechner, Y. Kunihashi, T. Dollinger, P. Olbrich, C. Schönhuber, I. Caspers, V. V. Bel'kov, L. E. Golub, D. Weiss, K. Richter, J. Nitta, and S. D. Ganichev, Phys. Rev. B **86**, 081306(R) (2012).

[20] A. Sasaki, S. Nonaka, Y. Kunihashi, M. Kohda, T. Bauernfeind, T. Dollinger, K. Richter, and J. Nitta, Nat. Nanotechnol. **9**, 703 (2014).

[21] Y. S. Chen, S. Fält, W. Wegscheider, and G. Salis, Phys. Rev. B **90**, 121304(R) (2014).

[22] N. Yamaguchi and F. Ishii, Appl. Phys. Express **10**, 123003 (2017).

[23] M. A. U. Absor, F. Ishii, H. Kotaka, and M. Saito, Appl. Phys. Express **8**, 073006 (2015).

[24] M. A. U. Absor and F. Ishii, Phys. Rev. B **99**, 075136 (2019).

[25] H. Ai, X. Ma, X. Shao, W. Li, and M. Zhao, Phys. Rev. Mater. **3**, 054407 (2019).

[26] R. Fei, W. Kang, and L. Yang, Phys. Rev. Lett. **117**, 097601 (2016).

[27] S. Barraza-Lopez, T. P. Kaloni, S. P. Poudel, and P. Kumar, Phys. Rev. B **97**, 024110 (2018).

[28] T. P. Kaloni, K. Chang, B. J. Miller, Q.-K. Xue, X. Chen, S.-H. Ji, S. S. P. Parkin, and S. Barraza-Lopez, Phys. Rev. B **99**, 134108 (2019).

[29] W. Wan, C. Liu, W. Xiao, and Y. Yao, Appl. Phys. Lett. **111**, 132904 (2017).

[30] P. Z. Hanakata, A. Carvalho, D. K. Campbell, and H. S. Park, Phys. Rev. B **94**, 035304 (2016).

[31] J. P. Perdew, K. Burke, and M. Ernzerhof, Phys. Rev. Lett. **77**, 3865 (1996).

[32] T. Ozaki, H. Kino, J. Yu, M. J. Han, N. Kobayashi, M. Ohfuti, F. Ishii, T. Ohwaki, H. Weng, and K. Terakura, http://www.openmx-square.org/ (2009).

[33] N. Troullier and J. L. Martins, Phys. Rev. B **43**, 1993 (1991).

[34] T. Ozaki, Phys. Rev. B **67**, 155108 (2003).

[35] T. Ozaki and H. Kino, Phys. Rev. B **69**, 195113 (2004).

[36] G. Theurich and N. A. Hill, Phys. Rev. B **64**, 073106 (2001).

[37] M. A. U. Absor, I. Santoso, Harsojo, K. Abraha, H. Kotaka, F. Ishii, and M. Saito, Phys. Rev. B **97**, 205138 (2018).

[38] M. A. U. Absor, H. Kotaka, F. Ishii, and M. Saito, Phys. Rev. B **94**, 115131 (2016).

[39] M. A. U. Absor, I. Santoso, Harsojo, K. Abraha, H. Kotaka, F. Ishii, and M. Saito, J. Appl. Phys. **122**, 153905 (2017).

[40] M. A. U. Absor, H. Kotaka, F. Ishii, and M. Saito, Jpn. J. Appl. Phys. (1962–1981) **57**, 04FP01 (2018).

[41] L. C. Gomes and A. Carvalho, Phys. Rev. B **92**, 085406 (2015).

[42] I. Appelbaum and P. Li, Phys. Rev. B **94**, 155124 (2016).

[43] G. Henkelman and H. Jónsson, J. Chem. Phys. **113**, 9978 (2000).

[44] R. D. King-Smith and D. Vanderbilt, Phys. Rev. B **47**, 1651 (1993).

[45] L. Xu, M. Yang, S. J. Wang, and Y. P. Feng, Phys. Rev. B **95**, 235434 (2017).

[46] W. Yao, E. Wang, H. Huang, K. Deng, M. Yan, K. Zhang, K. Miyamoto, T. Okuda, L. Li, Y. Wang, H. Gao, C. Liu, W. Duan, and S. Zhou, Nat. Commun. **8**, 14216 (2017).

[47] Q. Liu, Y. Guo, and A. J. Freeman, Nano Lett. **13**, 5264 (2013).

[48] S. Singh and A. H. Romero, Phys. Rev. B **95**, 165444 (2017).

[49] L. L. Tao and E. Y. Tsymbal, Nat. Commun. **9**, 2763 (2018).

[50] G. Fiori, F. Bonaccorso, G. Iannaccone, T. Palacios, D. Neumaier, A. Seabaugh, S. K. Banerjee, and L. Colombo, Nat. Nanotechnol. **9**, 768 (2014).

[51] J. H. Haeni, P. Irvin, W. Chang, R. Uecker, P. Reiche, Y. L. Li, S. Choudhury, W. Tian, M. E. Hawley, B. Craigo, A. K. Tagantsev, X. Q. Pan, S. K. Streiffer, L. Q. Chen, S. W. Kirchoefer, J. Levy, and D. G. Schlom, Nature (London) **430**, 758 (2004).

[52] K. Chang, J. Liu, H. Lin, N. Wang, K. Zhao, A. Zhang, F. Jin, Y. Zhong, X. Hu, W. Duan, Q. Zhang, L. Fu, Q.-K. Xue, X. Chen, and S.-H. Ji, Science **353**, 274 (2016).

[53] D. Di Sante, P. Barone, R. Bertacco, and S. Picozzi, Adv. Mater. **25**, 509 (2013).

[54] M. Kim, J. Im, A. J. Freeman, J. Ihm, and H. Jin, Proc. Natl. Acad. Sci. USA **111**, 6900 (2014).

[55] J. Rudge, H. Xu, J. Kolthammer, Y. K. Hong, and B. C. Choi, Rev. Sci. Instrum. **86**, 023703 (2015).

[56] V. Edelstein, Solid State Commun. **73**, 233 (1990).

[57] P. Gambardella and I. M. Miron, Philos. Trans. R. Soc., A **369**, 3175 (2011).

[58] C. Xiao, F. Wang, S. A. Yang, Y. Lu, Y. Feng, and S. Zhang, Adv. Funct. Mater. **28**, 1707383 (2018).

[59] B. Liu, M. Niu, J. Fu, Z. Xi, M. Lei, and R. Quhe, Phys. Rev. Mater. **3**, 054002 (2019).